NJC

Check for updates

Development of a novel SBA-15 templated mesoporous reduced graphitic oxide composite for high performance supercapacitors and fabrication of its device by an electrospinning technique†

Satishkumar R. Naik, Anand I. Torvi, Divya D. Achari and
Mahadevappa Y. Kariduraganavar ᴰ *

A novel synthetic route is formulated for the development of mesoporous reduced graphitic oxide (RGO)–silica composites by wrapping SBA-15 between the graphene oxide (GO) layers followed by a chemical reduction process. To prepare the Santa Barbara Amorphous (SBA-15) grafted graphene oxide, amino groups are grafted onto SBA-15, fabricated through a sol–gel technique using Pluronic P-123 as a template, tetraethyl orthosilicate as a silica source and pre-prepared graphene oxide as an additive. The formation of a mesoporous channel with an average pore diameter of 3.14 nm and a high specific surface area of ~10.58 m² g⁻¹ was confirmed by N_2 adsorption–desorption. Raman spectroscopy data displayed an increase in the I_D/I_G ratio of GO upon reduction indicating the creation of structural defects. Further, scanning electron microscopic analysis revealed the formation of a regular and ordered rod-like structure and transmission electron microscopic analysis confirmed the wrapping of the SBA-15 channel between GO layers. The conductance of the composites is measured by the four probe method. The three-electrode cell in an aqueous electrolyte shows a high specific capacitance of 533.3 F g⁻¹ with a high capacitance retention of 91% even after 2500 cycles. The composite delivers an energy and power density of 74.06 W h kg⁻¹ and 8.33 kW kg⁻¹, respectively, and these properties are much superior to those of graphene based supercapacitors reported in the literature. The fabricated supercapacitor device using the fibres developed by an electrospinning technique showed a high specific capacitance of 165.2 F g⁻¹, with a high energy density of 22.94 W h kg⁻¹. These electrochemical performances clearly indicate that mesoporous reduced graphene oxide could be used as a promising electrode material in supercapacitors for electrochemical energy storage.

Introduction

Globally, in the past few decades, there has been an ever increasing demand for the development of environment friendly and efficient energy storage devices. Growing demands in digital communication, electric vehicles and other devices that require electrical energy at high power levels in relatively short pulses have prompted a considerable interest in supercapacitors.[1–5] Supercapacitors are one of the important innovations in the field of electrical energy storage devices in view of their high specific power, long cycle-life stability, fast charging and safety as compared to rechargeable batteries.[6–11] Nevertheless, the main disadvantage of supercapacitors is the low energy density which is significantly lower than that of lithium ion rechargeable batteries. In addition, the currently available commercial supercapacitors have failed to possess sufficient power density to meet the present demand.

The commercially available supercapacitor devices are mostly based on the electrical double layer (EDL) charge storage mechanism and thus high surface area carbon materials have been extensively investigated.[12–14] These materials possess high power density owing to the formation of an EDL, but lack energy density. Therefore, the main criterion in the development of supercapacitors is to promote high energy density while retaining high power density as well as cycle-life stability.[15–17] Increasing the

*Department of Chemistry, Karnatak University, Dharwad 580 003, India.
E-mail: kariduraganavarmy@kud.ac.in, mahadevappayk@gmail.com;
Fax: +91-836-2771275; Tel: +91-9448590765*
† Electronic supplementary information (ESI) available: Details on the electrical conductivity of the developed composites, electrochemical measurements of the developed composites, dimensions and the SEM images of the electrospunned electrode. See DOI: 10.1039/c9nj02958c

cell voltage is an effective way to achieve high energy density and specific capacitance. In addition, high surface area and porous structures provide a beneficial way to obtain high energy density for carbonaceous electrode materials.

Recently, great efforts have been put forward to achieve the above-mentioned criteria, which include using several metal–organic frameworks in view of their high surface area and large pore volume.[18–21] Various asymmetric supercapacitor systems, such as graphene–MnO_2,[22] activated carbon–$Ni(OH)_2$,[23] carbon nanotube–MnO_2[24] and RGO–MnO_2–RGO,[25] have attracted great attention, owing to their significant improvement in energy density. Unfortunately, these assemblies still have restricted performance in terms of their sacrificed power density. Another promising strategy to improve the energy density was developed with three-dimensional porous nano-architectures, such as MnO_2–$NiCo_2O_4$ and graphene–Co_3O_4, through the direct growth of these materials on nickel foam using a hydrothermal or chemical vapour deposition method.[26–29] However, the complex fabrication process of these methods limits their practical utility especially for large-scale energy storage applications. Similarly, the development of hierarchical carbon materials is also one among the potential methods to address the energy density challenge in supercapacitor research, but they commonly suffer from the disadvantages of complicate synthetic methods and generation of a high ratio of macropores.[30–32] To address these, activated carbons with a high surface area have been widely used as electrode materials for supercapacitors and in such materials the uncontrollable pore geometry and pore size led to micropores, which in turn hindered the transportation of electrolyte ions under high-rate operation.[33] Another approach, namely, the carbide-derived-carbon (CDC) technique, can produce porous electrode materials with different mesopore–micropore ratios.[34,35] However, the chlorination of carbide at high temperature is more hazardous.

It is also realized that the capacitive performance of electrodes largely depends on the morphology, porosity and crystallinity of the electrode materials and especially the porous structure is favourable for effective ion and electron transport. Power density is sensitively dependent on the ion transport resistance inside the pores. The abundant micropores severely impede the ion transport owing to large resistance and hence lower the power density.[36,37] To optimize this, it is highly desired to generate mesopores as transport channels with minimum ion transport resistance. The high surface area and porous framework can increase the electrode–electrolyte interfacial contact and reduce the diffusion resistance during the charge–discharge process, and thus enhance the specific capacitance and cycle-life stability.[38]

Understanding the pros and cons of electrode materials and their structures, we present a novel synthetic route for the synthesis of SRG composites by wrapping different weights of SBA-15 in a fixed amount of graphene oxide followed by reduction of graphene oxide through a chemical method. The developed composites were designated as SRG-1, SRG-2, SRG-3, SRG-4 and SRG-5. To understand the suitability of the electrolyte, we performed cyclic voltammetry measurements in

1 M KOH, NaOH and LiOH electrolyte systems and systematically investigated their electrochemical properties for energy storage. In view of the superior electrochemical performance exhibited in the KOH electrolyte, we have kept KOH as a constant electrolyte system for further electrochemical studies. Among the five developed composites, SRG-3 demonstrated the highest specific capacitance, power density, energy density and cycle-life stability. These results were discussed based on porosity, surface area, mobility of ions, *etc.* Considering the performance of SRG-3, we have fabricated a supercapacitor device by developing fibres using an electrospinning technique and investigated its electrochemical performance systematically.

Experimental

Materials

Triblock Pluronic P-123 copolymer (EO20-PO70-EO20, BASF; $M_n \sim 5800$), tetraethyl orthosilicate, 3-aminopropyltriethoxysilane, N,N'-dicyclohexylcarbodiimide and polycaprolactone ($M_w \sim 14\,000$) were obtained from Sigma-Aldrich Chemie, GmbH, Germany. The natural graphite flake (~ 325 mesh, $\geq 99.8\%$ purity) was purchased from Alfa Aesar, Massachusetts, United States. Hydrogen peroxide (H_2O_2, $\geq 30\%$), potassium permanganate ($KMnO_4$), sodium nitrate ($NaNO_3$), toluene, N,N'-dimethylformamide (DMF) and sulfuric acid (H_2SO_4, 95–98%) were procured from S. D. Fine Chemicals Ltd, Mumbai, India. Hydrazine monohydrate was purchased from E. Merck Ltd, Mumbai, India. All the chemicals were of reagent grade and were used without further purification. Double distilled water was used throughout the study.

Preparation of graphitic oxide

Graphitic oxide (GO) was prepared by employing the modified Hummers' method.[39] Briefly, concentrated H_2SO_4 (92 ml), natural graphite (2 g) and $NaNO_3$ (2 g) were added into a 500 ml round bottom flask placed in an ice bath. To this, $KMnO_4$ (12 g) was added portion-wise for about 30 min with constant stirring. After stirring for 2 h, the reaction flask was transferred to a water bath and maintained at a temperature between 35 and 40 °C. After stirring for another 4 h, 200 ml of distilled water was added to the reaction mixture and the temperature was raised close to 100 °C and the mixture was stirred for 30 min. During stirring, the solution turned to brown. To this, around 20 ml of H_2O_2 was added until the colour of the solution changed to yellow. After centrifugation of the solution at 6000 rpm for 15 min, the solid was separated and washed several times with 0.1 M HCl and distilled water alternatively. The resulting GO was rinsed repeatedly with deionized water until the solution attained neutral pH. The obtained GO was subjected to exfoliation using ultrasonication for 30 min and then dried at around 40 °C under vacuum.

Synthesis of SBA-15

In a typical synthesis of highly ordered mesoporous SBA-15,[40] 12 g of triblock Pluronic P-123 copolymer was dissolved in

100 ml of distilled water and to this, 200 ml of 2 M HCl was added under stirring at ambient temperature (30 °C) and further stirred for 2 h. To this homogeneous solution, 27 g of tetraethyl orthosilicate was added and stirred at 40 °C overnight. The resulting gel was kept for crystallization under static hydrothermal conditions at 110 °C for 48 h in a Teflon lined autoclave reactor. The crystallized SBA-15 was filtered, washed with distilled water and dried. It was then subjected to calcination at 550 °C for 6 h to remove the unreacted template.

Preparation of amine functionalized mesoporous silica

The amine functional groups were introduced at the pore surface of the mesoporous silica as described by Zhang et al.[41] Briefly, SBA-15 (1 g) and 3-aminopropyltriethoxysilane (5 ml) were added into a 250 ml round bottom flask containing 100 ml of toluene under a nitrogen atmosphere and refluxed for 12 h. The resulting functionalized material was filtered, washed thoroughly with toluene and dried at around 80 °C to yield NH_2-SBA-15 as a hybrid material.

Synthesis of GO-SBA-15

The GO dispersion was prepared by sonicating GO in 100 ml of DMF for 30 min. To this, NH_2-SBA-15 and N,N'-dicyclohexylcarbo-

diimide (DCC) were added and the resulting reaction system was kept on a water bath at 60 °C for 24 h. The resulting product (GO-SBA-15) was filtered and washed with DMF followed by ethanol, and dried at 50 °C under vacuum. The composition of NH_2-SBA-15 was varied in the range of 0.01 to 0.2 g by keeping the weight of GO constant. Based on the amount of NH_2-SBA-15, the resulting composites of GO-SBA-15 were designated as SGO-1, SGO-2, SGO-3, SGO-4 and SGO-5. The details are presented in Table 1.

Synthesis of RGO-SBA-15

RGO-SBA-15 was synthesised by a chemical conversion method. In a typical procedure, 0.1 g of SGO-1 was dispersed in 50 ml of distilled water. To this, 0.1 ml of hydrazine monohydrate was added. The resulting mixture was heated for 1 h at around 95 °C. The product thus obtained was washed several times with distilled water to remove the excess hydrazine monohydrate and dried at 80 °C under vacuum to obtain RGO-SBA-15 in powder form and the same was designated as SRG-1. The same procedures were employed for SGO-2, SGO-3, SGO-4 and SGO-5, and were respectively designated as SRG-2, SRG-3, SRG-4 and SRG-5.

The preparation scheme of GO, SBA-15, GO-SBA-15 and SRG is illustrated in Fig. 1.

Device fabrication

For the purpose of fabrication of the supercapacitor device, an electrospinning technique was employed for the preparation of the electrode. In a typical procedure, 1 g of polycaprolactone (PCL) was initially dissolved by stirring in 7.5 ml of chloroform overnight at room temperature and to this, 2.5 ml of methanol was added and stirred for another two hours to obtain a clear viscous solution. To the resulting clear PCL solution, 0.1 g of

Table 1 Preparation of GO based composites

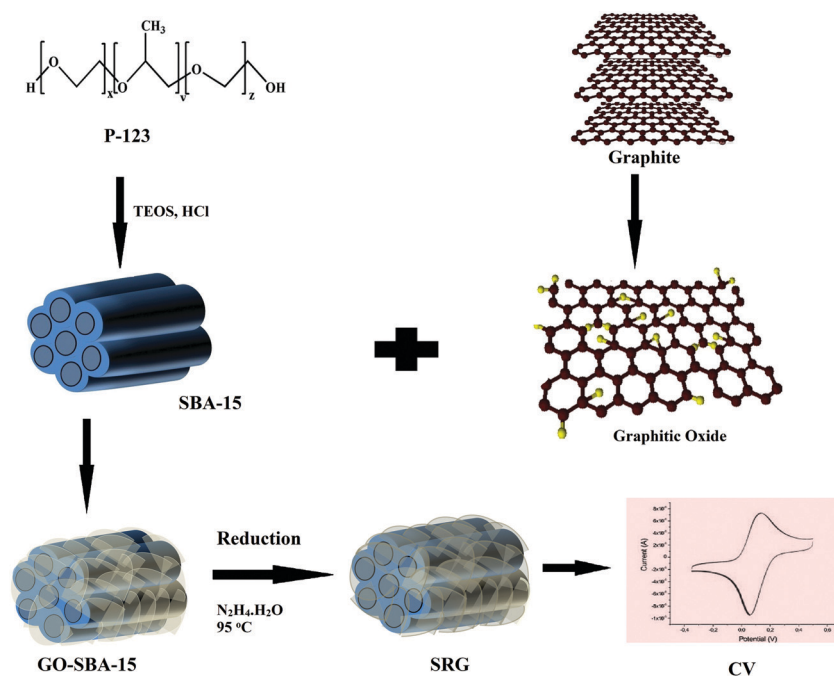| Weight of GO (g)	Weight of NH_2-SBA-15 (g)	Weight of DCC (g)	Weight ratio	Composites
0.04	0.01	0.04	1 : 0.25	SGO-1
0.04	0.02	0.04	1 : 0.5	SGO-2
0.04	0.04	0.04	1 : 1	SGO-3
0.04	0.1	0.04	1 : 2.5	SGO-4
0.04	0.2	0.04	1 : 5	SGO-5

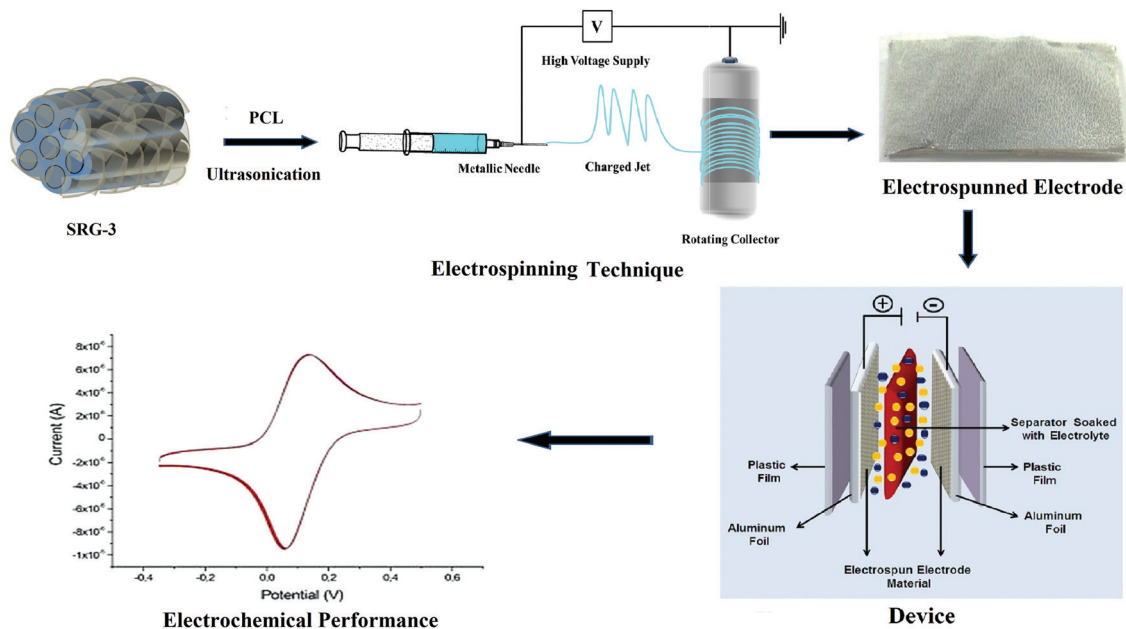**Fig. 1** Preparation scheme of GO, SBA-15, GO-SBA-15 and SRG.

Fig. 2 Fabrication of a supercapacitor device from the SRG-3 electrode material.

SRG-3 was added and dispersed homogeneously using an ultrasonicator and 5 ml of this solution was loaded in a plastic syringe and placed on a horizontal electrospinning set-up for the development of fibres. An electric potential was applied to the metallic needle (13.08 diameter and 3.2 cm length). The fibres were collected on a rotating collector covered with aluminium foil. The spinning was performed at room temperature (27 °C) with a relative humidity of 27%. The optimized experimental conditions are as follows: applied voltage 14 kV, solution flow rate 1 μl s^{-1}, distance of the tip of the needle to the collector 20 cm and duration of spinning 5 min. The aluminium foil with spun fibres was directly used as the electrode for the fabrication of the device.

The schematic representation of the fabricated supercapacitor is included in Fig. 2. The fabrication of the device was done as follows: two pieces of electrospun aluminium foil with a dimension of 2.5 cm width and 5 cm length were employed as shown in Fig. S5 (ESI†). The SEM images of the electrospun electrode material are presented in Fig. S6 (ESI†). The foils were attached to a double-sided adhesive tape for providing reinforcement. The two pieces of the copper wire were fixed by a screw for electrical contact at the end of the electrodes. The electrodes were overlapped together face to face and sandwiched by a piece of cellulose paper wetted with 1 M KOH electrolyte. The device was finally subjected to the encapsulation process for lamination. The photo image of the fabricated device is shown in Fig. 3.

Characterization

Fourier transform infrared (FT-IR) spectroscopy. The wrapping of SBA-15 in the GO sheets and the chemical reduction of GO were confirmed by using a FTIR spectrometer (Nicolet, Impact-410, USA). The samples were ground well to make KBr pellets under

Fig. 3 The photo image of the fabricated sandwich-type device.

a hydraulic pressure of 600 kg cm^{-2} and spectra were recorded in the range of 500–4000 cm^{-1}.

Raman spectroscopy. The Raman spectra of GO, SBA-15 and SRG composite were recorded using a Jobin-Yvon Triax 550 with a liquid N$_2$ cooled CCD detector (Horiba). The excitation wavelength of 532 nm was focused onto the sample through a modified epi-illuminator of a 50i Nikon microscope. The 50× microscope objective having a numerical aperture of 0.45 was used to focus the incident light. The scattered light was collected in 180° backscattering geometry.

Thermogravimetric analysis (TGA)

The thermal stability of GO, SBA-15 and SRG composite was investigated using a PerkinElmer TGA/DTA thermogravimetric analyzer (TA Instruments, SDT Q600, Waters LLC, New Castle, Delaware, USA). For each record, the weight of the samples employed was about 6–8 mg and the samples were heated from

ambient temperature to 800 °C at a heating rate of 10 °C min^{-1} under a nitrogen atmosphere.

Differential scanning calorimetry (DSC)

The thermal properties of GO, SBA-15 and SRG composite were studied using a differential scanning calorimeter (TA Instruments, DSC Q20, Waters LLC, New Castle, Delaware, USA). The sample weights ranged from 6 to 8 mg and the samples were heated from ambient temperature to 300 °C at a heating rate of 10 °C min^{-1} under a nitrogen atmosphere.

Scanning electron microscopy (SEM)

The surface morphology of SBA-15 and SRG composite was examined using a scanning electron microscope (Hitachi, S-3400N, Japan). Before photographing, all the samples were vacuum dried and sputtered with a conductive layer (400 Å) of gold.

Transmission electron microscopy (TEM)

The formation of hexagonal channels of SBA-15 and the wrapping of SBA-15 channels between GO flakes were examined using a transmission electron microscope (Jeol, JM 2100, Japan). An extremely small amount of material was suspended in ethanol to obtain a slightly turbid solution and the solution was ultrasonicated to disperse the particles. A drop of the solution was then taken out and cast on carbon-coated grids of 200 meshes. The coated grid was then dried and fixed in the specimen holder for the measurements.

Atomic force microscopy (AFM)

The surface morphology of GO and the developed SRG composite was studied using an atomic force microscope (Nanosurf, Model easyScan 2 Flex AFM, USA).

Brunauer–Emmett–Teller analysis (BET)

The porosity of SBA-15 and SRG composite was estimated using a Brunner–Emmett–Teller (BET) surface area analyzer (BET Surface Area Analyzer, Micromeritics, Japan). The apparent pore volume of the samples was determined by a single point measurement based on the adsorbed nitrogen amount at a relative pressure of P/P_0. N$_2$ adsorption isotherms obtained were used to calculate the pore size distribution and the specific surface area using the Barrett–Joyner–Halenda (BJH) method and Brunauer–Emmett–Teller (BET) theory.

Electrical conductivity study

The AC conductivity of SRG composites was measured using a four point probe setup (SES Instruments, DF-P-02, India) at room temperature. The detailed procedure is given in the ESI.†

Electrochemical study

The cyclic voltammograms of different composites were recorded using an electrochemical workstation in a three-electrode cell (CH Instruments Inc., CHI 608E, USA). An Ag/AgCl electrode was used as the reference electrode, and a glassy carbon electrode and platinum wire were employed as the working and counter electrodes, respectively. Electrochemical impedance spectroscopy and galvanostatic charge–discharge measurements were carried out using a potentiostat/galvanostat (CH Instruments Inc., CHI 608E, USA).

Results and discussion

Fourier transform infrared (FT-IR) spectroscopy

FTIR spectroscopy was employed in order to investigate the structure and functional groups in GO, SBA-15 and SRG composite. The FT-IR spectra of graphite, GO, SBA-15 and SRG composite are presented in Fig. 4. In the spectrum of graphene, the bands that appeared at 3431 and 1620 cm^{-1} could be attributed to the O–H stretching vibrations and the skeletal vibration of unoxidized C=C bonds (sp^2), respectively. After the oxidation of graphene, apart from these two vibrations, three new representative bands were observed in the spectrum of GO at 1726, 1399 and 1222 cm^{-1}, which were assigned to the stretching bands of C=O, C–OH and C–O–C, respectively. These characteristic bands clearly indicate the introduction of oxygen-containing functional groups onto the surface of graphite upon oxidation. A broad band that appeared between 3000 and 3700 cm^{-1} was attributed to the stretching and bending vibrations of –OH groups. This is mainly due to the adsorbed water molecules on the surface of GO, and suggested that GO exhibited a strong hydrophilic nature. In the FTIR spectrum of SBA-15, the bands that appeared at 2930 and 2850 cm^{-1} were respectively attributed to symmetric and anti-symmetric stretching vibrations of CH$_2$ groups.[42,43] The bands that appeared at 1402 and 1414 cm^{-1} were assigned to the deformation of –OH and the stretching of C–O bonds of –COOH groups, respectively.[44,45] The characteristic band at 1630 cm^{-1} was attributed to the restricted vibrations of the C=C bond in
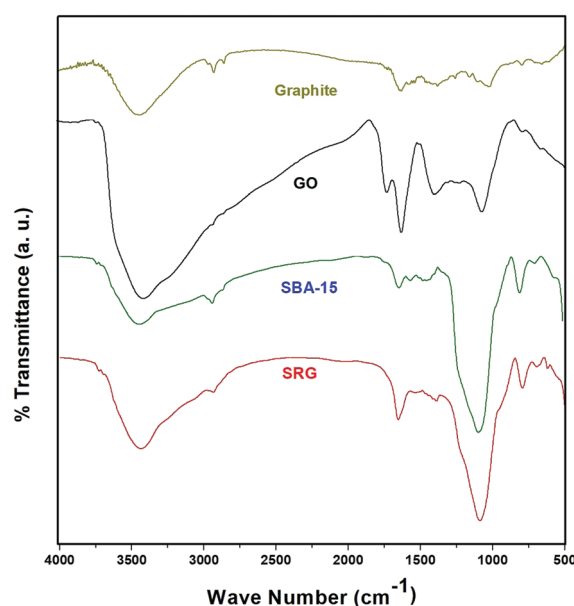

Fig. 4   FTIR spectra of graphite, GO, SBA-15 and SRG composite.

the plane of carbon atoms.[46,47] Similarly, the characteristic bands that appeared at around 1250 and 3400 cm^{-1} were attributed to the Si–O–Si and O–H stretching vibrations.

By comparing the FTIR spectra of GO and SRG, it is observed that the characteristic band of C=O that appeared at 1726 cm^{-1} showed a much lower intensity for SRG. After the chemical reduction, the bands assigned for the oxygen functional groups were reduced significantly in the spectrum of SRG suggesting successful reduction of GO.

Raman spectroscopy

Raman spectroscopy is a prevailing tool to study the characteristics of carbon based materials.[48,49] The main feature in the Raman spectra of graphitic carbon based materials, such as graphene o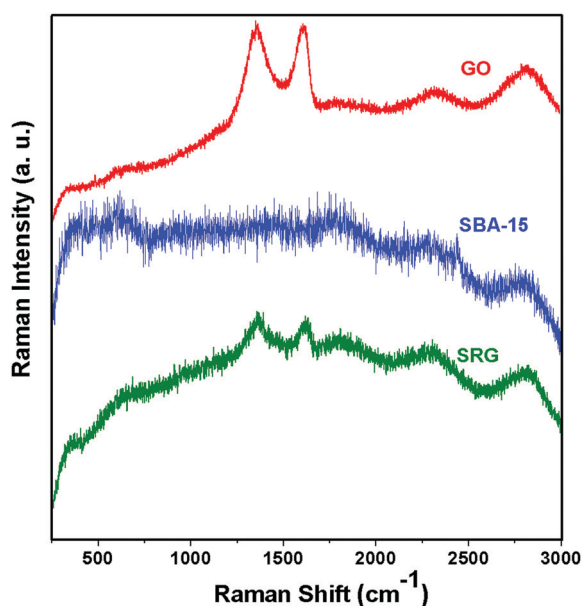xide and reduced graphene oxide, is the occurrence of G and D peaks. The Raman spectrum of GO shows the presence of a very strong D peak at 1370 cm^{-1} with an intensity comparable to that of the G peak at 1565 cm^{-1} (Fig. 5). The intense D peak along with a large bandwidth suggests the significant structural disorder in GO.[50,51]

The characteristic peak of the D band that appeared at 1370 cm^{-1} corresponded to the vibration of sp^3 carbon atoms, while the G band that appeared at 1565 cm^{-1} was attributed to the in-plane vibration of sp^2 carbon atoms.[52,53]

The ratio of intensity of I_D:I_G for GO was found to be 1.00, and this ratio was increased to 1.38 for the SRG composite. After the reduction of GO, the intensity ratio of I_D:I_G was found to be higher than that of GO and is firstly due to the higher degree of disorderness.[54–58] This is expected, owing to the decreased sp^2-carbon domains in the SRG composite. Secondly, the generation of vacant lattice sites in the matrix is also responsible for the reduction of the intensity ratio. This is mainly due to the removal of the oxygen atom, which leads to structural defects during the reduction of GO.

Thermogravimetric analysis

The thermal stability and degradation behaviour of SBA-15, GO and SRG composite were investigated by TGA under a nitrogen atmosphere and the thermograms thus obtained are presented in Fig. 6a.

From the TGA profile of GO, it is observed that the first weight loss observed between 60 and 110 °C corresponded to the weight loss of absorbed water molecules. The second and major weight loss that occurred between 120 °C and 250 °C was attributed to the loss of functional groups in GO. Beyond 250 °C, the graphene oxide gradually underwent decomposition. This suggests that the functional groups underwent decomposition at a lower temperature while the destruction of the carbon backbone took place at higher temperature.

The TGA profile of SBA-15 shows a major weight loss up to 110 °C, which corresponds to desorption of physically absorbed water molecules from the mesoporous structure of SBA-15.

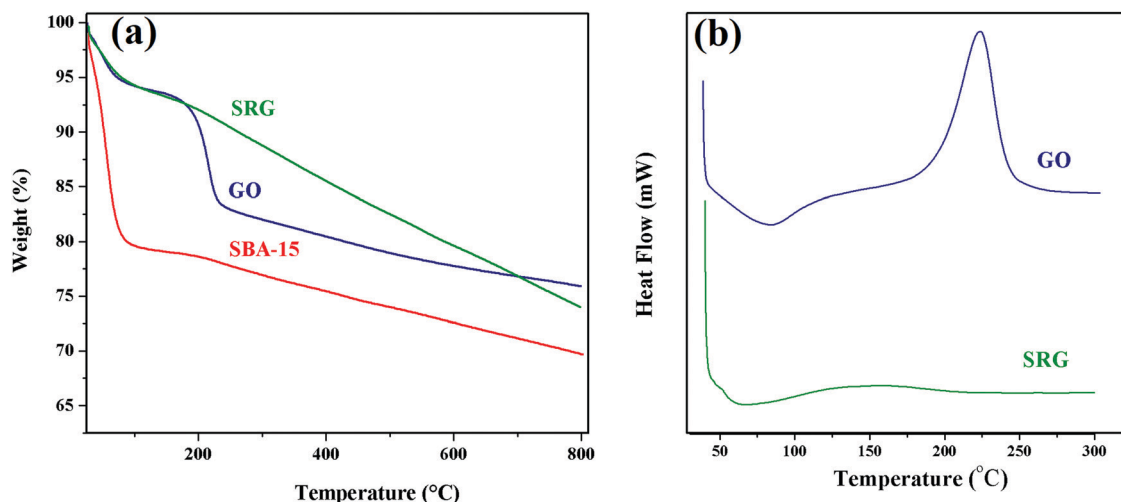Fig. 5 Raman spectra of GO, SBA-15 and SRG composite.

Fig. 6 (a) TGA thermograms of GO, SBA-15 and SRG composite; (b) DSC thermograms of GO and SRG composite.

In the range from 110 to 215 °C, a small weight loss was observed and this was attributed to desorption of chemisorbed water molecules from the silica surface. Beyond 250 °C, SBA-15 underwent decomposition gradually and this was attributed to decomposition of silanol groups.

The thermogram of the SRG composite shows that the composite underwent first degradation loss between ambient temperature and 110 °C, and this was attributed to loss of physically absorbed water molecules. Beyond 110 °C, the SRG composite started degradation almost linearly with temperature, and this is due to decomposition of functionalised SBA-15. From the thermograms of GO and SRG, it is clearly evident that the SRG sample started decomposing at a much higher temperature than GO. At 300 °C, only 12% weight loss occurred for the SRG composite while 22.5 and 17.5% weight loss occurred for SBA-15 and GO, respectively. This suggests that the developed SRG composite demonstrated an excellent thermal stability as compared to GO and SBA-15.

Differential scanning calorimetry

The thermal behaviour of GO and SRG composite was also investigated using DSC and the thermograms are presented in Fig. 6b. From the thermogram of GO, we observed an exothermic peak at around 230 °C, which was attributed to the evolution of CO and CO_2 from GO owing to the destruction of oxygenated functional groups.[59] The absence of this characteristic peak in the DSC thermogram of SRG is evidence for the successful reduction of GO.

Scanning electron microscopy

The morphology of GO, SBA-15 and SRG composite was examined by scanning electron microscopy and the resulting images of GO (a), SBA-15 (b) and SRG composite (c and d) are shown in Fig. 7. From the images of Fig. 7b, we observed a regular and ordered rod-like structure of SBA-15. These are in good agreement with the SBA-15 reported by Stucky *et al.*[60] The surface of GO is quite smooth and partially transparent as shown in Fig. 7a. During the formation of GO-SBA-15, the pore channels of SBA-15 with a well-ordered mesoporous structure were wrapped up in the GO sheets. Later, the GO is reduced to RGO and the resulting composite (RGO-SBA-15) was designated as SRG. After the wrapping of SBA-15 between the GO flakes and followed by its chemical reduction, the SBA-15 channels still retained their rod-like structure. The typical lamellar structure of GO changed to a curly structure during the chemical reduction process. This is clearly seen from the SEM images presented in Fig. 7(c and d). This nanocomposite with a mesoporous channel structure allows easy transport of electrolyte ions.

Transmission electron microscopy

The TEM images of SBA-15 and SRG composites at different magnifications are presented in Fig. 8. From the images
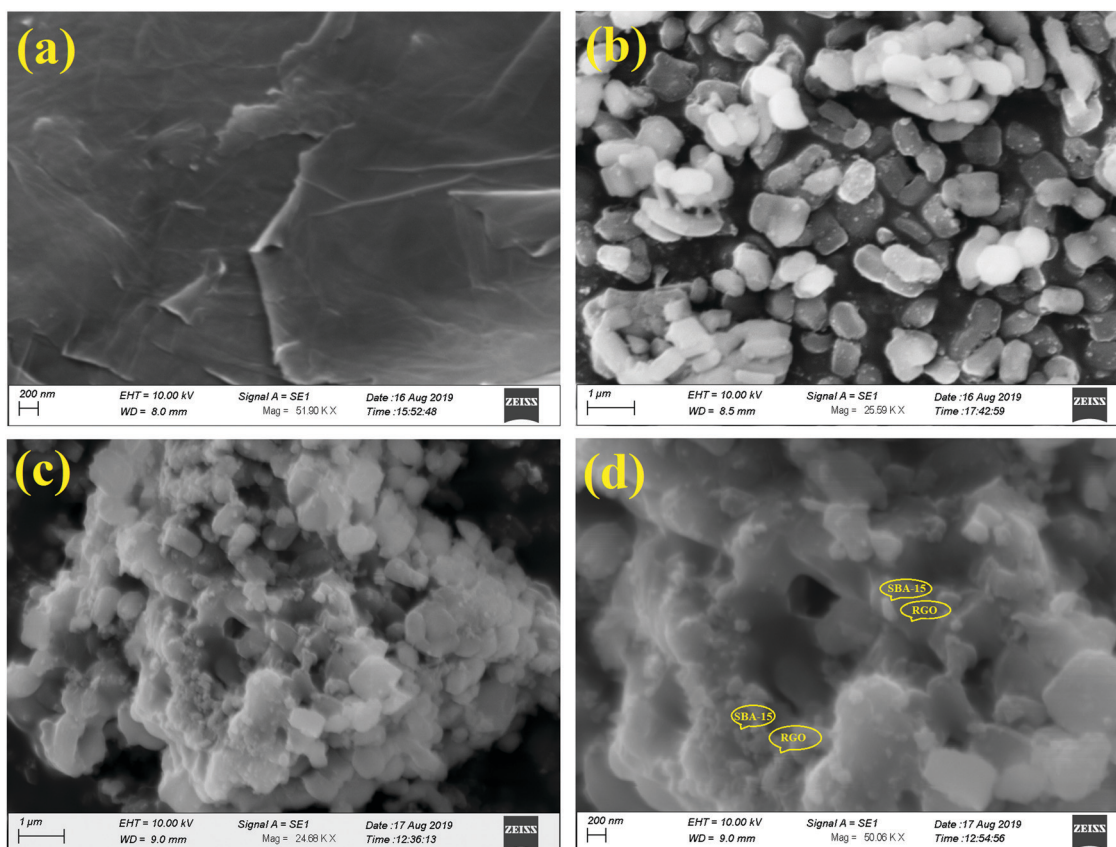

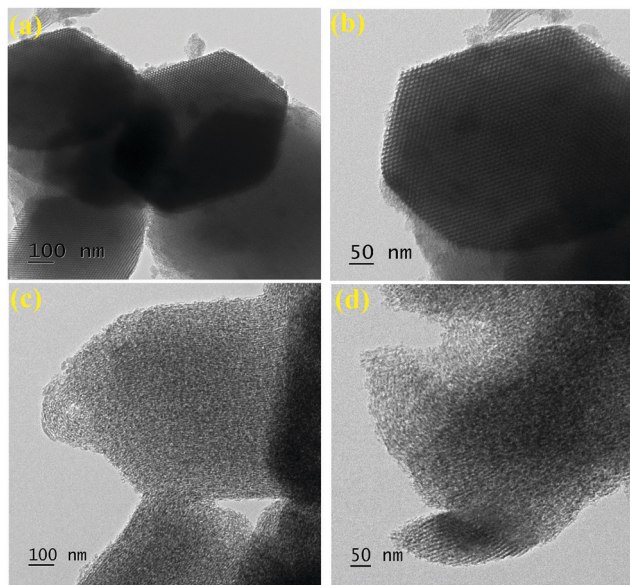Fig. 7 SEM images of GO (a), SBA-15 (b) and SRG composite (c and d).

Fig. 8   TEM images of SBA-15 (a and b) and SRG composite (c and d).

(Fig. 8a and b), it is observed that SBA-15 showed a network of parallel channels. The intercalated GO layer appeared as a dark object between the channels of SBA-15. However, the visibility of SBA-15 network channels in the SRG composite was not clear as noticed from Fig. 8(c and d). This is due to the overlapping of the hexagonal structure. This clearly suggests the wrapping of the SBA-15 channel between GO layers. It is therefore concluded that SBA-15 is a good template as we could control the layer thickness and the growth direction, and thus prevent the bulk aggregation of graphene oxide. From the images of SRG,

we can also conclude that there is an easy access of the electrolyte in the outer and inner surfaces of the electrode material.

Atomic force microscopy

The surface morphology of GO and the developed SRG composite was studied using an atomic force microscope and the resulting micrographs are displayed in Fig. 9. The surface morphology is clearly distinguishable with a spike like shape in the case of 3D tapping mode of GO (Fig. 9d). However, a smooth layer was observed in the 3D tapping mode in the case of SRG (Fig. 9f), which indicates the overlap of the hexagonal structure of SBA-15 channels by GO layers. The black dots observed in the 2D tapping mode image of the SRG composite (Fig. 9c) clearly indicate the channel like structure. This could provide better accessibility for the electrode and electrolyte.

BET study

To study the porosity of SBA-15 and SRG composite, N_2 adsorption isotherms were measured using the activated samples at 77 K. The nitrogen adsorption–desorption isotherms of SBA-15 and SRG composite are given in Fig. 10. The textural properties of SBA-15 and SRG composite based on BET results are summarized in Table 2. In both the samples, the absorption and desorption isotherms (Fig. 10a and b) followed the type-IV behaviour. Both pore diameter and volume decreased from SBA-15 to SRG, and accordingly, the surface area was decreased. This clearly indicates that the wrapping of SBA-15 between GO layers and its reduction was successful. Further, the pore diameter of SRG was found to be 3.14 nm, suggesting that a well defined array of the regular mesoporous structure of SBA-15 was retained. Similarly, the capillary condensation steps of both SBA-15 and
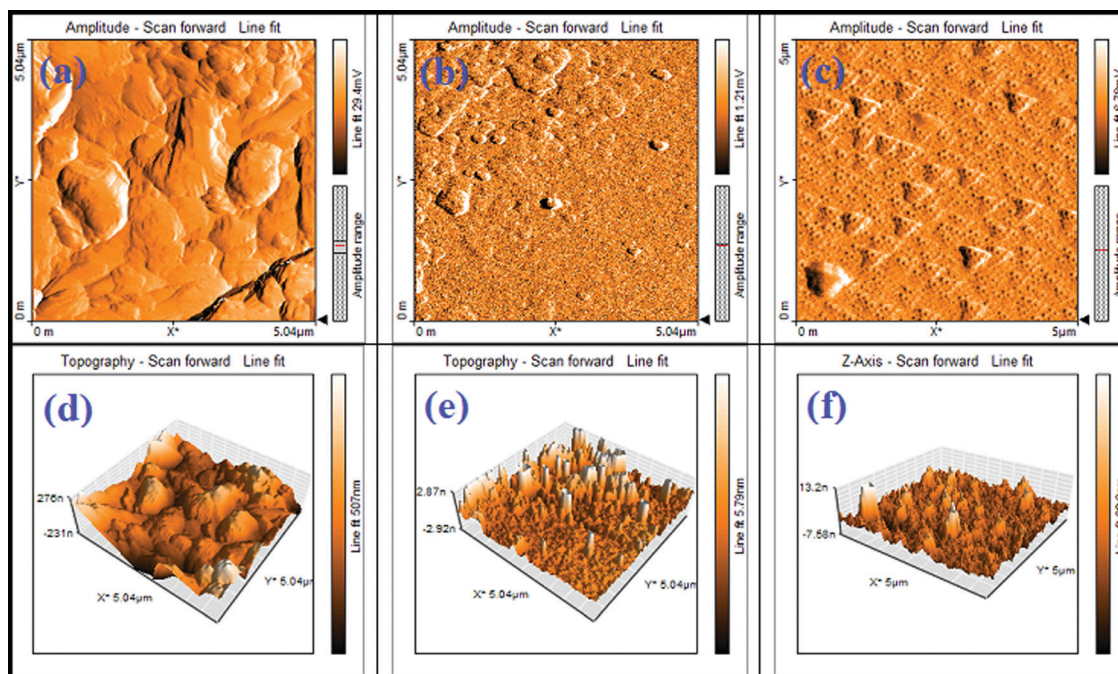

Fig. 9   2D and 3D AFM images of GO (a and d), SBA-15 (b and e) and SRG composite (c and f).
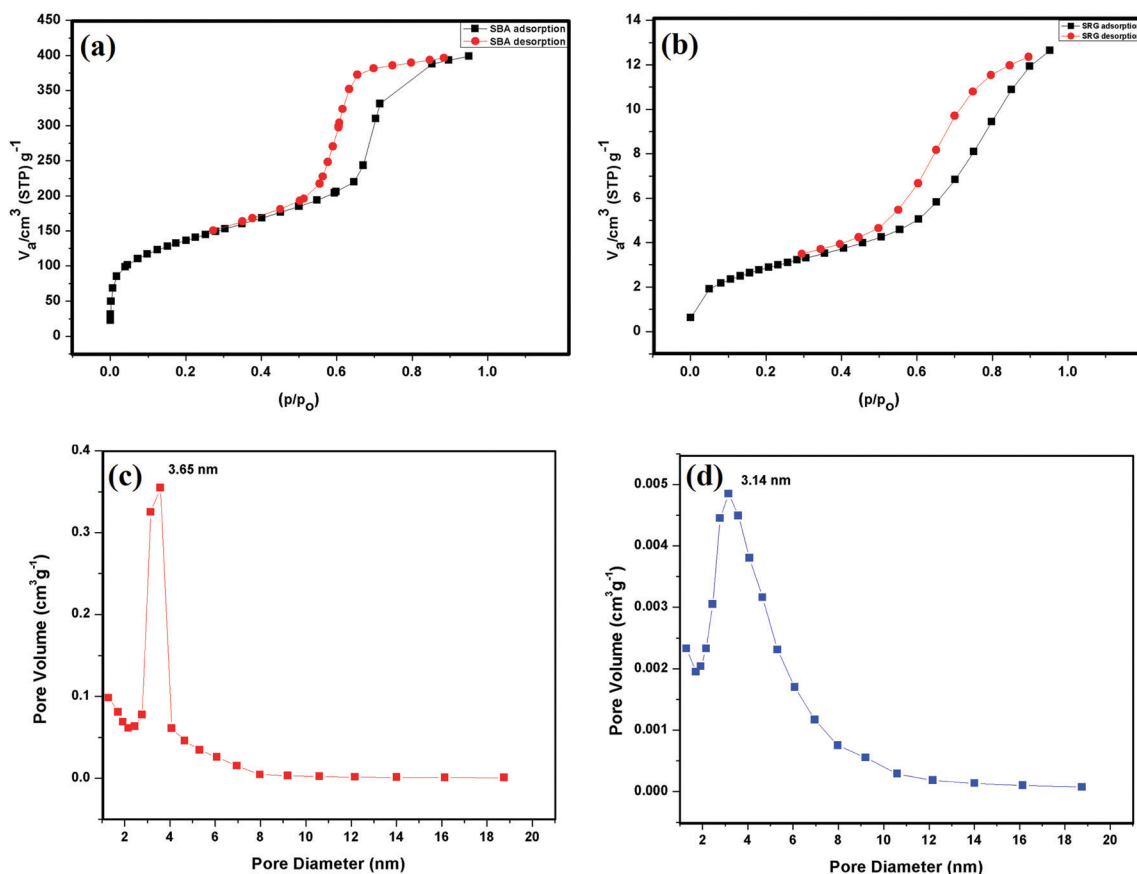
Fig. 10   (a and b) The N$_2$ adsorption desorption isotherms of SBA-15 and SRG composite; (c and d) the pore size distribution of SBA-15 and SRG composite obtained from adsorption measurements.

SRG isotherms were found to be in the range of 0.6–0.7, indicating the uniformity of the pore size. All these pieces of evidence contribute to the overall electrochemical performance of the developed SRG electrode.

Electrical conductivity study

The electrical conductivity is one of the prime requirements in achieving better electrochemical performance. Thus, the electrical conductivity of all the developed composites was determined using a four-point probe method and the data are presented in Fig. S1 (ESI†). As the weight of SBA-15 was increased, the electrical conductivity increased up to the SRG-3 composite and showed a maximum electrical conductivity of 3.676 S cm^{-1}, and beyond this, the electrical conductivity decreased with a further increase in the weight of SBA-15. This is because, as the weight of SBA-15 was increased, the conducting network channels were created initially in the developed composites, and thus conductivity was greatly enhanced. However, when SBA-15 was increased beyond the weight ratio of 1 : 1, the structure of channels collapsed and led to dissipation of conductivity in the matrix. As a result, the conductivity of SRG-4 and SRG-5 was decreased.

Electrochemical performance of SRG composites

To study the electrochemical behaviour of all the composites, cyclic voltammetry (CV) experiments were performed using a three electrode configuration over a potential window of −1 V to +1 V at a scan rate of 2 mV s^{-1} in 1 M KOH electrolyte as shown in Fig. S2(a) and S3 (ESI†). The specific capacitance values of SRG-1, SRG2, SRG-3, SRG-4 and SRG-5 nanocomposites obtained from cyclic voltammetry (CV) measurements are given in Table S1 (ESI†).

From the data, it is clear that the specific capacitance value obtained for the nanocomposite SRG-1 was found to be 161.0 F g^{-1} at 2 mV s^{-1}. This value gradually increased and reached a maximum specific capacitance of 305.0 F g^{-1} for the nanocomposite SRG-3 with the increasing content of SBA-15. Upon further increasing the content of SBA-15 the specific capacitance gradually decreased and reached 231.9 F g^{-1} for the nanocomposite SRG-5.

From the CV experiments, it is observed that among the developed composite electrodes, SRG-3 showed the highest current response. Further, to choose the appropriate electrolyte, we measured the cyclic voltammograms of the SRG-3 electrode in 1 M KOH, NaOH and LiOH and the resulting cyclic voltammograms are presented in Fig. S2(b) (ESI†).

SRG-3 was studied by cyclic voltammetry at different scan rates from 2 mV s^{-1} to 100 mV s^{-1} in the KOH electrolyte and the obtained cyclic voltammograms are displayed in Fig. 12(a). The specific capacitance values calculated from all the cyclic voltammograms are given in Table S2 (ESI†).

Table 2 The textural properties of SBA-15 and SRG composite

Substrate	Surface area (m² g⁻¹)	Pore diameter (nm)	Pore volume (cm³ g⁻¹)
SBA-15	473.9	3.65	6.172×10^{-1}
SRG	10.58	3.14	0.195×10^{-1}

From the data, it is noticed that the KOH electrolyte system showed the highest current response among the electrolytes chosen. This could be explained based on the hydrated diameter of the cations. It is noted that the average pore diameter of the SRG composite determined from the BET equation was found to be 3.14 nm (Table 2). Improvements in supercapacitor energy storage characteristics depend strongly on the relative size of pores and the effective relative size of electrolyte ions.[61] The developed mesopores are large enough to accommodate K⁺ and OH⁻ ions. From a simple geometric consideration, ∼100% of the measured mesopores of the SRG channel structure are available for accommodating K⁺ ions (hydrated diameter = 3.31 Å; Fig. 11a). In comparison, for Na⁺ ions (hydrated diameter = 3.58 Å) only ∼50% of the pores are accessible (Fig. 11b), while for Li⁺ ions (hydrated diameter = 3.82 Å) only 25% are accessible (Fig. 11c). Accordingly, cycling in an aqueous KOH electrolyte is predicted to yield the highest energy and power performance from mesoporous electrodes. Thus, the comparison of the electrochemical performance of the developed composite in different alkaline electrolytes with different hydrated cation diameters can provide mechanistic insights into the relationship between pore size and the size of the electrolyte. As a result, KOH ions could easily transport through the channels of SRG composites during the electrochemical process. In contrast, in the case of larger hydrated cations such as Na⁺ and Li⁺ their transport through the channels is limited which restricts their access to the active surface of the mesopores. Among the SRG composites, SRG-3 demonstrated an excellent electrochemical performance. Similarly, the KOH electrolyte showed the highest current response among the electrolytes employed. Thus, we have selected only the SRG-3 composite and performed further electrochemical studies in the KOH electrolyte.

The cyclic voltammograms of the SRG-3 electrode measured from 2 mV s⁻¹ to 100 mV s⁻¹ are presented in Fig. 12(a). The cyclic voltammograms of the SRG-3 composite were distorted rectangular in shape suggesting that the developed composite

behaved as an ideal electrical double layer capacitor. The galvanostatic charge–discharge (GCD) analysis of SRG-3 was carried out in the KOH electrolyte and the resulting curves are presented in Fig. 12(b) and Fig. S4 (ESI†). The GCD curves are not symmetric, and in fact are deviated from the symmetric nature. This is due to the diffusion-limited mobility of electrolyte ions in the pores of the electrode. All the GCD curves are of almost the same shape at all current densities, showing that the electrode material has ideal capacitive behaviour.

The specific capacitance (C_{sp}) values of the SRG-3 composite calculated from the charge–discharge curves are presented in Table S3 (ESI†). The calculated specific capacitance values are plotted as a function of current density as shown in Fig. 12(c). From the plot, it is observed that the specific capacitance decreased monotonously with increasing current density. The specific capacitance of the SRG-3 composite was found to be 533.3 F g⁻¹ at 1.0 mA g⁻¹, which is higher than those of porous activated carbons[62–64] and materials obtained from chemically reduced graphene oxides.[65,66] Similarly, the specific capacitance of the SRG-3 composite is even higher than the specific capacitance values reported for materials with high surface areas. For instance, Xu et al.[67] and Gutsev et al.[68] respectively achieved a BET surface area of 3405 m² g⁻¹ and 600 m² g⁻¹, but no proportional increase in capacitance was observed for the developed graphene based electrode materials. They obtained a specific capacitance of only up to 200 F g⁻¹ even though the surface area is one of the major criteria for high specific capacitance. Further, the specific capacitance value of the SRG-3 composite decreased gradually with increasing current density and reached a minimum value of 266.7 F g⁻¹ at a high current density of 2 mA g⁻¹. The decrease in specific capacitance at higher current densities is attributed to the inadequate availability of electro-active materials during the high charge–discharge process.

The long term cycle-life stability of SRG-3 was investigated by performing repeated charge–discharge cycles at a current density of 1.0 mA g⁻¹ and the results are presented in Fig. 12(d). It is found that, even after 2500 cycles at a current density of 1.0 mA g⁻¹, around 91% of capacitance was retained, suggesting that the developed SRG-3 composite demonstrated an excellent cycle-life stability as an electrode material. The typical triangular shapes of the GCD curves measured for the first and last few cycles are also included in the inset of Fig. 12(d), which indicate
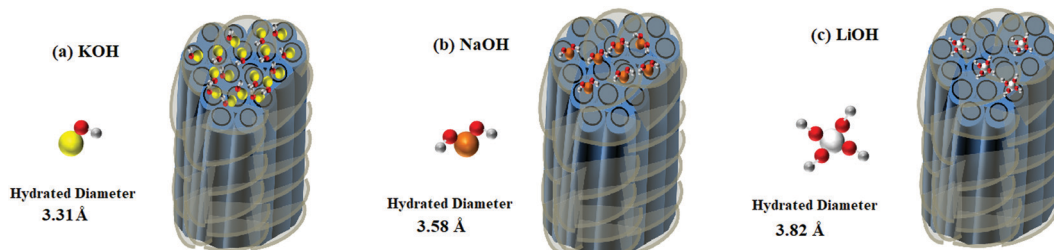

Fig. 11 Schematic representation of accommodation of hydrated cations in the pores of SRG composites; from the simple geometric consideration, ∼100%, ∼50% and ∼25% of pores could accommodate (a) K⁺ (hydrated diameter = 3.31 Å), (b) Na⁺ (hydrated diameter = 3.58 Å) and (c) Li⁺ (hydrated diameter = 3.82 Å, respectively).
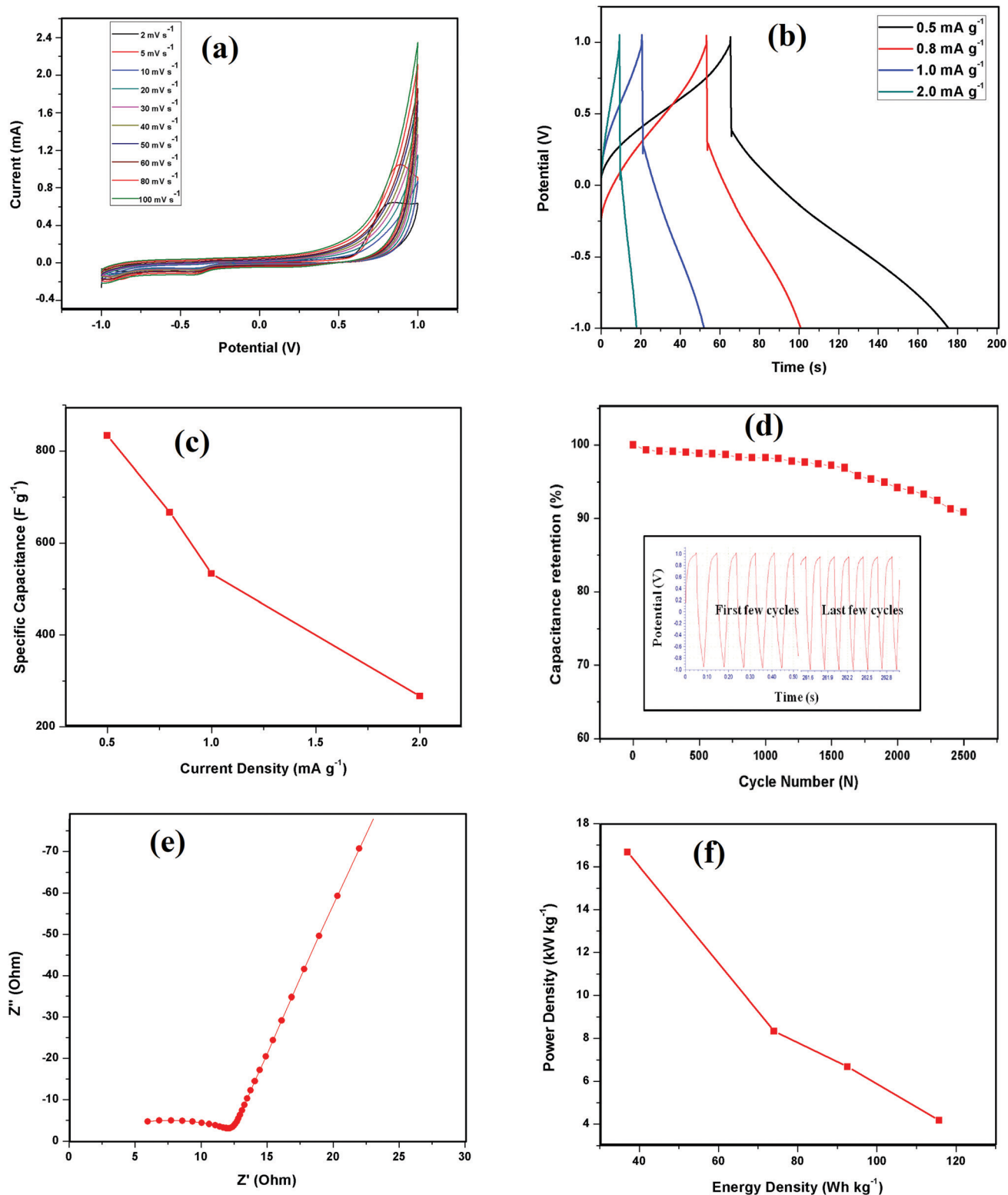
Fig. 12 Electrochemical performance of the SRG-3 composite. (a) Cyclic voltammograms of the SRG-3 composite measured from 2 mV s^{-1} to 100 mV s^{-1} in 1 M KOH electrolyte; (b) GCD curves of the SRG-3 composite measured at different current densities; (c) specific capacitance of the SRG-3 composite as a function of current density; (d) cycle-life performance of the SRG-3 composite over 2500 charge–discharge cycles at 1.0 mA g^{-1} current density. Inset: Galvanostatic charge–discharge curves of the SRG-3 composite for the first and last few cycles; (e) the Nyquist plot of the SRG-3 composite electrode; (f) the Ragone plot of the SRG-3 composite showing good energy density and power density retention.

the retention of their shapes even after 2500 cycles. This again confirms the good capacitive properties of the developed electrode material.

The higher capacitance in the initial cycles is mainly due to the availability of more surface sites and the consequent enhanced wettability of the electrode by the KOH activation process. In fact, this is an outstanding performance demonstrated among graphene based EDLC supercapacitors. For instance, the MnO_2–graphene–graphene based supercapacitor exhibited only 72% retention of specific capacitance after 1000 cycles.[69]

The performance of the electrode system was further investigated by electrochemical impedance spectroscopy (EIS) in the frequency range of 100 kHz to 1 Hz with an ac voltage amplitude of 5 mV. The Nyquist plot represents the imaginary component (Z') against the real component (Z'') of the impedance as shown in Fig. 12(e). The arch in the high frequency region of the Nyquist plot is attributed to the diffusion of ions at the electrode/electrolyte interfaces.[70–73] The plot indicates that in the low frequency region, nearly vertical lines were observed, suggesting that the developed composite electrode behaved as an ideal capacitor. Fig. 12(f) shows the Ragone plot to demonstrate the electrochemical performance of the proposed work. From the plot, it is clear that the energy density reached 115.74 W h kg^{-1} at a power density of 4.17 kW kg^{-1}. Similarly, the energy density was found to be 37.04 W h kg^{-1} at a very high power density of 16.67 kW kg^{-1}. The SRG-3 composite exhibited higher energy density (74.06 W h kg^{-1}) compared to other graphene based supercapacitor electrode materials such as onion-like carbon (5.7 W h kg^{-1}),[74] RGO–CuO–PEDOT nanocomposite (14.15 W h kg^{-1}),[75] functionalised RGO–PANI nanofiber composite films (16.3 W h kg^{-1}),[76] RGO/Mn_3O_4 (27.41 W h kg^{-1}),[77] 3D-RGO/$NiMoO_4$ nanocomposite (32.36 W h kg^{-1}),[78] RGO/TiO_2 nanosheet (32.454 W h kg^{-1}),[79] RGO–CNT–Co_3S_4 nanocomposite (43.5 W h kg^{-1}),[80] graphene–polyaniline (49.58 W h kg^{-1})[81] and porous RGO–$NiMn_2O_4$–PANI ternary nanohybrid (70 W h kg^{-1}).[82]

Moreover, the energy density of the SRG-3 composite electrode is much higher than that of the commercialized activated carbon (3–5 W h kg^{-1})[83] while its power density is maintained at 8.33 kW kg^{-1} at a current density of 1.0 mA g^{-1}. All these results ascertain that the SRG-3 composite electrode in the KOH electrolyte was able to provide high energy density while delivering higher power. These superior features of SRG-3 were mainly attributed to the factors such as the incorporation of GO in the SBA-15 channel, which effectively prevents the agglomeration of GO and consequently provides more surface sites for intercalation of aqueous K^+ ions; the resulting vibrant electronic conduction and short diffusion paths, which improve the performance of the positive electrode; and a broad potential range of SRG-3 (2 V), which increases the energy density as it is proportional to the square of cell voltage. These factors are very well supported from the conclusions drawn by Singh *et al.*[84] Due to the high and stable functional groups of SRG-3 with the channel structure of SBA-15, the K^+ and OH^- ions can intercalate into the interlayer under the action of an electric field, which further expands the layer spacing and gradually increases the electrolyte-accessible surface area and thus facilitates the diffusion of ions.

Based on the excellent performance of the SRG-3 composite electrode we are prompted to compare the specific capacitance of SRG-3 with the RGO based composites reported in the literature. The specific capacitance values are summarised in Table 3. From the data, it is observed that among the composite materials reported in the literature, the RGO–PANI composite exhibited the highest specific capacitance value of 524.4 F g^{-1}. This value is relatively lower compared to that of the SRG-3 composite reported here. This signifies that the SRG-3 composite developed here is superior to RGO based electrode materials.

Electrochemical performance of the fabricated device

Considering the superior electrochemical performance of the developed SRG-3 electrode material, we have developed a new

Table 3 Comparison of the specific capacitance (C_{sp}) of RGO based composites and the developed SRG-3 composite

Materials	Specific capacitance (F g^{-1})	Ref.
RGO from pollen grains (Pgs)	27.1	85
RGO–PANI composite	72.0	86
RGO–CuO–PEDOT nanocomposite	156.7	76
RGO from natural graphite	170	87
RGO from microwave exfoliation (MEGO)	200	88
RGO foam	224	89
RGO–TiO_2 nanosheet	233.67	79
RGO-nanostructured Fe_2O_3	235	90
RGO by reduction and exfoliation of GO under an air atmosphere	299	91
Microwave reduced graphene oxide (MrGO)	302	92
RGO–ZnO nanocomposite	312.0	93
RGO–Cu_2O–Ni(OH)$_2$ nanocomposites	318	94
RGO–Mn_3O_4 composite	342.5	77
RGO–MoS_2 heterostructure	387.6	95
RGO decorated polyaniline hollow fiber	449.0	96
RGO–PANI composite	524.4	97
N-Doped RGO–PANI hydrogel	514.3	98
RGO–SBA mesoporous nanocomposite	533.3	Present work

Note: PANI – polyaniline; TiO_2 – titanium oxide; CuO – copper oxide; PEDOT – poly(3,4-ethylenedioxythiophene); ZnO – zinc oxide; Mn_3O_4 – manganese oxide; MoS_2 – molybdenum disulfide; WS_2 – tungsten disulfide; CdS – cadmium sulphide; CeO_2 – cerium oxide; MOF – metal–organic framework; CoP – cobalt(III) phosphide.
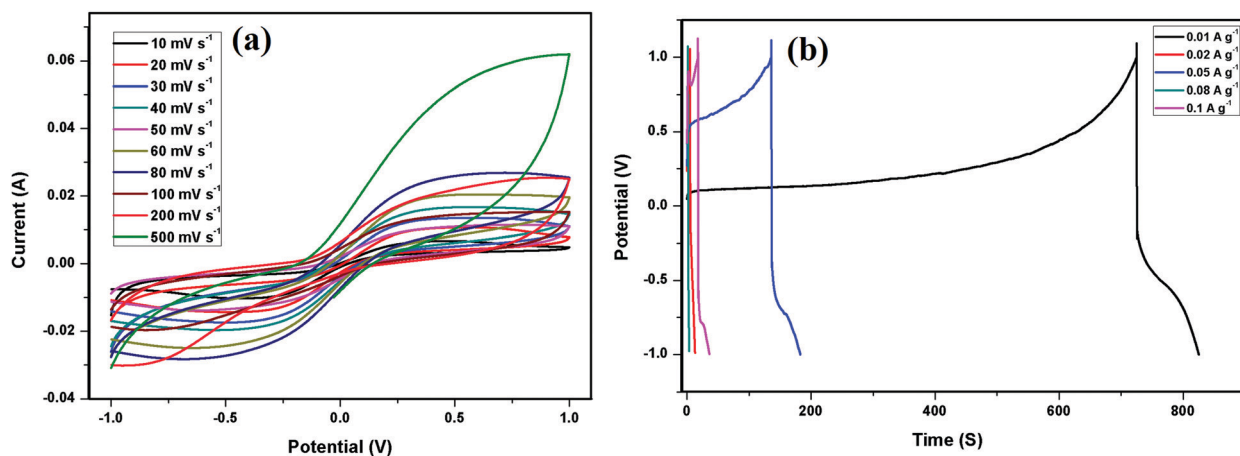
Fig. 13   Electrochemical performance of the fabricated device. (a) The cyclic voltammograms of the device at different scan rates; (b) the GCD curves of the supercapacitor device at different current densities.

supercapacitor device by employing the electrospinning technique and systematically investigated its electrochemical performance. To assess the electrochemical performance, the newly fabricated supercapacitor device was subjected to cyclic voltammetry and galvanostatic charge–discharge analysis. The supercapacitor device exhibited rectangular shaped curves at all scan rates as shown in Fig. 13a, suggesting a typical EDLC-type behaviour. Similarly, the galvanostatic charge–discharge measurement was also carried out in the potential range between −1 V and +1 V at different current densities from 0.01 A g^{-1} to 0.1 A g^{-1} (Fig. 13b). It is noticed that the device exhibited triangular charge–discharge curves for all the current density values.

The specific capacitance was calculated from the GCD curves. At a current density of 0.05 A g^{-1}, the specific capacitance of the developed supercapacitor was found to be 162.5 F g^{-1}. Finally, we have also calculated the energy density and power density of the supercapacitor device. The device exhibited an extremely high energy density of 22.94 W h kg^{-1} with a power density of 124.9 W kg^{-1}. These findings highlight the potential of the fabricated supercapacitor device for energy storage applications.

Conclusions

In summary, a simple method was adopted to prepare the SRG composites by employing SBA-15 as a stable mesoporous structure. It is evident from the study that the mesoporous channels of SBA-15 were wrapped up between the layers of GO and subsequently reduced by a chemical method. Among the developed composites, the SRG-3 composite exhibited a typical channel structure with an average pore diameter of 3.14 nm and a moderate specific surface area of 10.58 m^2 g^{-1}. The SRG-3 composite also exhibited an excellent electrical conductivity as high as 3.68 S cm^{-1} with improved thermal stability. The specific capacitance of SRG-3 was found to be 533.3 F g^{-1}, with a high energy and power density of 74.06 W h kg^{-1} and 8.33 kW kg^{-1}, respectively, at 1 mA g^{-1} in 1 M KOH electrolyte. With regard to cycle-life stability, it was found that around

91% capacitance was retained even after 2500 cycles. The resulting excellent electrochemical performance of the composite was mainly due to reduced diffusion resistance owing to the introduction of a mesoporous channel structure and easy intercalation of K$^+$ and OH$^-$ into the interlayer of composites during the charge–discharge process. Thus, we concluded that the SRG-3 composite could be used as a promising electrode material for supercapacitor applications. Further, considering its high specific capacitance and good cycle-life stability, we have developed a new and easily fabricated supercapacitor device by employing an electrospinning technique and investigated its performance systematically. The fabricated device exhibited a specific capacitance of 162.5 F g^{-1} at a current density of 0.05 A g^{-1} with a high energy density of 22.94 W h kg^{-1} and a power density of 124.9 W kg^{-1}. In conclusion, the electrochemical performance of the developed supercapacitor device is promising for its potential application in electrochemical energy storage.

Nomenclature

GO	Graphitic oxide
RGO	Reduced graphitic oxide
EIS	Electrochemical impedance spectroscopy
CV	Cyclic voltammetry
GCD	Galvanostatic charge–discharge
EDLC	Electrochemical double layer capacitors
H$_2$O$_2$	Hydrogen peroxide
KOH	Potassium hydroxide
NaOH	Sodium hydroxide
LiOH	Lithium hydroxide
KMnO$_4$	Potassium permanganate
NaNO$_3$	Sodium nitrate
DMF	*N,N*-Dimethylformamide
PCL	Polycaprolactone
FTIR	Fourier transform infrared spectroscopy
TGA	Thermogravimetric analysis
DSC	Differential scanning calorimetry

SEM	Scanning electron microscopy
TEM	Transmission electron microscopy
AFM	Atomic force microscopy
BJH	Barrett–Joyner–Halenda
BET	Brunauer–Emmett–Teller
A	Ampere
mA	Milliampere
V	Volt
mV	Millivolt
nm	Nanometer
cm	Centimeter
$S\ cm^{-1}$	Siemens per centimeter
F	Farad
kg	Kilogram
kHz	Kilohertz
W h	Watt hour
kW	Kilowatt

Conflicts of interest

There are no conflicts of interest to declare.

Acknowledgements

References

1 B. E. Conway, *Electrochemical supercapacitors: scientific fundamentals and technological applications*, Plenum, New York, 1999, ch. 15.

2 Z. Yu, L. Tetard, L. Zhai and J. Thomas, *Energy Environ. Sci.*, 2015, **8**, 702–730.

3 X. Cao, Z. Yin and H. Zhang, *Energy Environ. Sci.*, 2014, **7**, 1850–1865.

4 Y. Ji, L. Huang, J. Hu, C. Streb and Y.-F. Song, *Energy Environ. Sci.*, 2015, **8**, 776–789.

5 A. Torvi, S. Naik and M. Kariduraganavar, *Chemical Data Collections*, 2018, **17–18**, 459–471.

6 L. F. Chen, Z. Y. Yu, J. J. Wang, Q. X. Li, Z. Q. Tan, Y. W. Zhu and S. H. Yu, *Nano Energy*, 2015, **11**, 119–128.

7 Q. Lu, Y. Chen, W. Li, J. G. Chen, J. Q. Xiao and F. Jiao, *J. Mater. Chem. A*, 2013, **1**, 2331–2336.

8 A. Torvi, B. Munavalli, S. Naik and M. Kariduraganavar, *Electrochim. Acta*, 2018, **282**, 469–479.

9 Y. Xu, I. Hennig, D. Freyberg, A. J. Strudwick, M. G. Schwab, T. Weitz and K. C.-P. Cha, *J. Power Sources*, 2014, **248**, 483–488.

10 F. Grote, Z. Y. Yu, J. L. Wang, S. H. Yu and Y. Lei, *Small*, 2015, **11**, 4666–4672.

11 H.-P. Cong, X.-C. Ren, P. Wang and S.-H. Yu, *Energy Environ. Sci.*, 2013, **6**, 1185–1191.

12 Y. Li, Z. Li and P. K. Shen, *Adv. Mater.*, 2013, **25**, 2474–2480.

13 C. Zheng, X. Zhou, H. Cao, G. Wang and Z. Liu, *J. Power Sources*, 2014, **258**, 290–296.

14 Y. Ma, C. Ma, J. Sheng, H. Zhang, R. Wang, Z. Xie and J. Shi, *J. Colloid Interface Sci.*, 2016, **461**, 96–103.

15 L. J. Xie, J. F. Wu, C. M. Chen, C. M. Zhang, L. Wan, J. L. Wang, Q. Q. Kong, C. X. Lv, K. X. Li and G. H. Sun, *J. Power Sources*, 2013, **242**, 148–156.

16 J. P. Zheng and T. R. Jow, *J. Electrochem. Soc.*, 1995, **142**(1), L6–L8.

17 H. Zhu, X. Wang, X. Liu and X. Yang, *Adv. Mater.*, 2012, **24**(48), 6524–6529.

18 B. Liu, H. Shioyama, T. Akita and Q. Xu, *J. Am. Chem. Soc.*, 2008, **130**, 5390–5391.

19 B. Liu, H. Shioyama, H. Jiang, X. Zhang and Q. Xu, *Carbon*, 2010, **48**, 456–463.

20 M. Hu, J. Reboul, S. Furukawa, L. Radhakrishnan, Y. Zhang, P. Srinivasu, H. Iwai, H. Wang, Y. Nemoto, N. Suzuki, S. Kitagawa and Y. Yamauchi, *Chem. Commun.*, 2011, **47**, 8124–8126.

21 L. Radhakrishnan, J. Reboul, S. Furukawa, P. Srinivasu, S. Kitagawa and Y. Yamauchi, *Chem. Mater.*, 2011, **23**, 1225–1231.

22 J. Cao, Y. Wang, Y. Zhou, J. H. Ouyang, D. Jia and L. Guo, *J. Electroanal. Chem.*, 2013, **689**, 201–206.

23 D. Cericolia, P. W. Ruch, R. Kotz, P. Novak and A. Wokaun, *Electrochem. Commun.*, 2010, **12**, 812–815.

24 P. C. Chen, G. Z. Shen, Y. Shi, H. T. Chen and C. W. Zhou, *ACS Nano*, 2010, **4**, 4403–4411.

25 Z. S. Wu, W. Ren, D. W. Wang, F. Li, B. Liu and H. M. Cheng, *ACS Nano*, 2010, **4**, 5835–5842.

26 T. Zhai, F. Wang, M. Yu, S. Xie, C. Liang, C. Li, F. Xiao, R. Tang, Q. Wu, X. Lu and Y. Tong, *Nanoscale*, 2013, **5**, 6790–6796.

27 G. Zhang and X. W. Lou, *Adv. Mater.*, 2013, **25**, 976–979.

28 Z. Chen, W. Ren, L. Gao, B. Liu, S. Pei and H. M. Cheng, *Nat. Mater.*, 2011, **10**, 424–428.

29 F. Zhang, C. Yuan, X. Lu, L. Zhang, Q. Che and X. Zhang, *J. Power Sources*, 2012, **203**, 250–256.

30 D. W. Wang, F. Li, M. Liu, G. Q. Lu and H. M. Cheng, *Angew. Chem., Int. Ed.*, 2009, **48**, 1525.

31 M. Q. Zhao, Q. Zhang, J. Q. Huang and F. Wei, *Adv. Funct. Mater.*, 2012, **22**, 675–694.

32 J. Biener, M. Stadermann, M. Suss, M. A. Worsley, M. M. Biener, K. A. Rose and T. F. Baumann, *Energy Environ. Sci.*, 2011, **4**, 656–667.

33 K. Xia, Q. Gao, J. Jiang and J. Hu, *Carbon*, 2008, **46**, 1718–1726.

34 C. Largeot, C. Portet, J. Chmiola, P. L. Taberna, Y. Gogosti and P. Simon, *J. Am. Chem. Soc.*, 2008, **130**, 2730–2731.

35 H. Wang and Q. Gao, *Carbon*, 2009, **47**, 820–828.

36 X. Yang, C. Cheng, Y. Wang, L. Qiu and D. Li, *Science*, 2013, **341**(6145), 534–537.

37 J. Park, S. B. Jo, Y. J. Yu, Y. Kim, J. W. Yang, W. H. Lee, H. H. Kim, B. H. Hong, P. Kim, K. Cho and K. S. Kim, *Adv. Mater.*, 2012, **24**(3), 407–411.

38 S. Stankovich, D. A. Dikin, R. D. Piner, K. A. Kohlhaas, A. Kleinhammes, Y. Jia, Y. Wu, S. T. Nguyen and R. S. Ruoff, *Carbon*, 2007, **45**, 1558–1565.

39 Y. Xu, H. Bai, G. Lu, C. Li and G. Shi, *J. Am. Chem. Soc.*, 2008, **130**, 5856–5857.

40 D. Zhao, Q. Huo, J. Feng, B. F. Chmelka and G. D. Stucky, *J. Am. Chem. Soc.*, 1998, **120**, 6024–6036.

41 L. X. Zhang, C. C. Yu, W. R. Zhao, Z. L. Hua, H. R. Chen, L. Li and J. L. Shi, *J. Non-Cryst. Solids*, 2007, **353**, 4055–4061.

42 L. Shahriary and A. A. Athawale, *Int. J. Energy Environ. Eng.*, 2014, **2**, 58–63.

43 T. Szabo, O. Berkesi and I. Dekany, *Carbon*, 2005, **43**, 3186–3189.

44 B. Ramezanzadeh, E. Ghasemi, M. Mahdavian, E. Changizi and M. H. M. Moghadam, *Chem. Eng. J.*, 2015, **281**, 869–883.

45 Y. Dong, J. Shao, C. Chen, H. Li, R. Wang, Y. Chi, X. Lin and G. Chen, *Carbon*, 2012, **50**, 4738–4743.

46 L. Chai, T. Wang, L. Zhang, H. Wang, W. Yang, S. Dai, Y. Meng and X. Li, *Carbon*, 2015, **81**, 748–757.

47 B. Zahed and H. H. Monfared, *Appl. Surf. Sci.*, 2015, **328**, 536–547.

48 M. Cheng, R. Yang, L. Zhang, Z. Shi, W. Yang, D. Wang, G. Xie, D. Shi and G. Zhang, *Carbon*, 2012, **50**, 2581–2587.

49 H. Tanaka, S. Obata and K. Saiki, *Carbon*, 2013, **59**, 472–478.

50 A. C. Ferrari, *Solid State Commun.*, 2007, **143**, 47–57.

51 A. C. Ferrari, J. C. Meyer, V. Scardaci, C. Casiraghi, M. Lazzeri, F. Mauri, S. Piscanec, D. Jiang, K. S. Novoselov, S. Roth and A. K. Geim, *Phys. Rev. Lett.*, 2006, **97**, 187401.

52 K. Ai, Y. Liu, L. Lu, X. Cheng and L. Huo, *J. Mater. Chem.*, 2011, **21**, 3365–3370.

53 N. A. Kumar, H.-J. Choi, Y. R. Shin, D. W. Chang, L. Dai and J.-B. Baek, *ACS Nano*, 2012, **6**, 1715–1723.

54 X.-Y. Peng, X.-X. Liu, D. Diamond and K. T. Lau, *Carbon*, 2011, **49**, 3488–3496.

55 G. T. S. How, A. Pandikumar, H. N. Ming and L. H. Ngee, *Sci. Rep.*, 2014, **4**, 5044.

56 C. Chen, M. Long, M. Xia, C. Zhang and W. Cai, *Nanoscale Res. Lett.*, 2012, **7**, 101.

57 M. Mishra, A. P. Singh, B. P. Singh and S. K. Dhawan, *RSC Adv.*, 2014, **4**, 25904–25911.

58 E. H. Lee, D. M. Hembree, G. R. Rao and L. K. Mansur, *Phys. Rev. B: Condens. Matter Mater. Phys.*, 1993, **48**, 15540–15551.

59 Z. A. Al-Othman, A review: fundamental aspects of silicate mesoporous materials, *Materials*, 2012, **5**, 2874–2902.

60 D. Margolese, J. A. Melero, S. C. Christiansen, B. F. Chmelka and G. D. Stucky, *Chem. Mater.*, 2000, **12**, 2448–2459.

61 C. Zhong, Y. Deng, W. Hu, D. Sun, X. Han, J. Qiao and J. Zhang, *Compatibility of electrolytes with inactive components of electrochemical supercapacitors*, CRC Press, 2016, pp. 255–274.

62 T. A. Centeno and F. Stoeckli, *Electrochim. Acta*, 2006, **52**, 560–566.

63 T. A. Centeno, M. Hahn, J. A. Fernández, R. Kötz and F. Stoeckli, *Electrochem. Commun.*, 2007, **9**, 1242–1246.

64 F. Stoeckli and T. A. Centeno, *J. Mater. Chem. A*, 2013, **1**, 6865–6873.

65 Y. Huang, J. Liang and Y. Chen, *Small*, 2012, **8**, 1805–1834.

66 Y. Zhu, S. Murali, W. Cai, X. Li, J. W. Suk, J. R. Potts and R. S. Ruoff, *Adv. Mater.*, 2010, **22**, 3906–3924.

67 H.-L. Jiang, B. Liu, Y.-Q. Lan, K. Kuratani, T. Akita, H. Shioyama, F. Zong and Q. Xu, *J. Am. Chem. Soc.*, 2011, **133**, 11854–11857.

68 Y. M. Shulga, S. A. Baskakov, Y. V. Baskakova, Y. M. Volfkovich, N. Y. Shulga, E. A. Skryleva, Y. N. Parkhomenko, K. G. Belay, G. L. Gutsev, A. Y. Rychagov, V. E. Sosenkin and I. D. Kovalev, *J. Power Sources*, 2015, **279**, 722–730.

69 Z. Lu, Q. Yang, W. Zhu, Z. Chang, J. Liu, X. Sun, D. G. Evans and X. Duan, *Nano Res.*, 2012, **5**, 369–378.

70 N. Zhu, W. Liu, M. Xue, Z. Xie, D. Zhao, M. Zhang, J. Chen and T. Cao, *Electrochim. Acta*, 2010, **55**, 5813–5818.

71 J. Song and M. Z. Bazant, *J. Electrochem. Soc.*, 2013, **160**, A15–A24.

72 A. Ehsani, M. G. Mahjani and M. T. Jafarian, *Turk. J. Chem.*, 2011, **35**, 735–743.

73 D. Antiohos, K. Pingmuang, M. Romano, S. Beirne, T. Romeo, P. Aitchison, A. Minett, G. Wallace, S. Phanichphant and J. Chen, *Electrochim. Acta*, 2013, **101**, 99–108.

74 K. Makgopa, P. M. Ejikeme, C. J. Jafta, K. Raju, M. Zeiger, V. Presser and K. I. Ozoemena, *J. Mater. Chem. A*, 2015, **3**, 3480–3490.

75 M. Ates, A. Garip, O. Yörük, Y. Bayrak, O. Kuzgun and M. Yildirim, *Plast., Rubber Compos.*, 2019, **48**, 168–184.

76 K. Jin, W. Zhang, Y. Wang, X. Guo, Z. Chen, L. Li, Y. Zhang, Z. Wang, J. Chen, L. Sun and T. Zhang, *Electrochim. Acta*, 2018, **285**, 221–229.

77 Y. Zhou, L. Guo, W. Shi, X. Zou, B. Xiang and S. Xing, *Materials*, 2018, **11**, 881.

78 S. A. Rastabi, R. S. Mamoory, F. Dabir, N. Blomquist, M. Phadatare and H. Olin, *Crystals*, 2019, **9**, 31.

79 S. Sundriyal, M. Sharma, A. Kaur, S. Mishra and A. Deep, *J. Mater. Sci.: Mater. Electron.*, 2018, **29**, 12754–12764.

80 A. Mohammadi, N. Arsalani, A. G. Tabrizi, S. E. Moosavifard, Z. Naqshbandi and L. S. Ghadimi, *Chem. Eng. J.*, 2018, **334**, 66–80.

81 M. K. Chini and S. Chatterjee, *FlatChem*, 2016, **1**, 1–5.

82 S. Sahoo, S. Zhang and J.-J. Shim, *Electrochim. Acta*, 2016, **216**, 386–396.

83 A. Burke and M. Miller, *J. Power Sources*, 2011, **196**, 514–522.

84 P. Ahuja, V. Sahu, S. K. Ujjain, R. K. Sharma and G. Singh, *Electrochim. Acta*, 2014, **146**, 429–436.

85 O. S. A. Rahman, V. Chellasamy, N. Ponpandian, S. Amirthapandian, B. K. Panigrahi and P. Thangadurai, *RSC Adv.*, 2014, **4**, 56910–56917.

86 Shruthi, K. Vighnesha, Sandhya, D. N. Sangeetha and M. Selvakumar, *Surf. Eng. Appl. Electrochem.*, 2018, **54**, 359–366.

87 B. Lobato, V. Vretenár, P. Kotrusz, M. Hulman and T. A. Centeno, *J. Colloid Interface Sci.*, 2015, **446**, 203–207.

88 Y. M. Shulga, S. A. Baskakov, Y. V. Baskakova, Y. M. Volfkovich, N. Y. Shulga, E. A. Skryleva, Y. N. Parkhomenko, K. G. Belay, G. L. Gutsev, A. Y. Rychagov, V. E. Sosenkin and I. D. Kovalev, *J. Power Sources*, 2015, **279**, 722–730.

89 H.-C. Tao, S.-C. Zhu, X.-L. Yang, L.-L. Zhang and S.-B. Ni, *Electrochim. Acta*, 2016, **190**, 168–177.

90 Q. Yang, R. Bi, K.-C. Yung and M. Pecht, *Electrochim. Acta*, 2017, **231**, 125–134.

91 S. M. B. Hosseinia, S. M. Baizaeea, H. R. Naderib and A. D. Kordi, *Appl. Surf. Sci.*, 2018, **427**, 507–516.

92 S. A. El-Khodary, G. M. El-Enany, M. El-Okr and M. Ibrahim, *Electrochim. Acta*, 2014, **150**, 269–278.

93 J. Jayachandiran, J. Yesuraj, M. Arivanandhan, A. Raja, S. Austin Suthanthiraraj, R. Jayavel and D. Nedumaran, *J. Inorg. Organomet. Polym. Mater.*, 2018, **28**, 2046–2055.

94 K. Wang, C. Zhao, S. Min and X. Qian, *Electrochim. Acta*, 2015, **165**, 314–322.

95 M. Saraf, K. Natarajan and S. Mobin, *ACS Appl. Mater. Interfaces*, 2018, **10**, 16588–16595.

96 F. Tabar, F. Sharif and S. Mazinani, *Polymer*, 2018, **154**, 80–89.

97 N. Chen, Y. Ren, P. Kong, L. Tan, H. Feng and Y. Luo, *Appl. Surf. Sci.*, 2017, **392**, 71–79.

98 Y. Zou, Z. Zhang, W. Zhong and W. Yang, *J. Mater. Chem. A*, 2018, **6**, 9245–9256.